

Primal-dual Newton methods in structural optimization

Ronald H. W. Hoppe · Christopher Linsenmann ·
Svetozara I. Petrova

Abstract We consider the numerical solution of optimization problems for systems of partial differential equations with constraints on the state and design variables as they arise in the optimal design of the shape and the topology of continuum mechanical structures. After discretization the resulting nonlinear programming problems are solved by an “all-at-once” approach featuring the numerical solution of the state equations as an integral part of the optimization routine. In particular, we focus on primal-dual Newton methods combined with interior-point techniques for an appropriate handling of the inequality constraints. Special emphasis is given on the efficient solution of the primal-dual

system that results from the application of Newton’s method to the Karush–Kuhn–Tucker conditions where we take advantage of the special block structure of the primal-dual Hessian. Applications include structural optimization of microcellular biomorphic ceramics by homogenization modeling, the shape optimization of electrorheological devices, and the topology optimization of high power electromotors.

1 Introduction

The optimization of the shape and the topology of continuum mechanical structures by means of a systematic, physically consistent design methodology is referred to as structural optimization. The design criteria are chosen according to a goal oriented operational behavior of the structures under consideration and typically lead to nonlinear objective functionals depending on the state variables describing the operational mode and the design variables determining the shape and the topology. The state variables are assumed to satisfy differential equations reflecting the underlying physical laws whereas technological aspects may give rise to further equality and inequality constraints on both the state and the design variables.

Although structural optimization can be traced back to the work of Bernoulli, Euler, Lagrange, and Saint-Venant, it became its own discipline during the second half of the last century when the rapid progress in electronic data processing required the development and implementation of highly efficient and robust algorithmic optimization tools (cf., e.g., the monographs by [1, 3, 4, 13, 14, 27, 28, 45, 48, 50, 55] and the references therein).

The first and the third author have been supported by the DFG within the Collaborative Research Center SFB 438 and within the Priority Program SPP 1095 under the Grants Ho 877/5-1 and Ho 877/5-2. The first author acknowledges further support by the BMBF under Grant 03HOM3A1.

Dedicated to Peter Deuffhard on the occasion of his 60th birthday.

R. H. W. Hoppe (✉)
Department of Mathematics,
University of Houston,
Houston, TX 77204-3008, USA
e-mail: hoppe@math.uni-augsburg.de

C. Linsenmann
Institute of Mathematics,
University of Augsburg,
86159 Augsburg, Germany

S. I. Petrova
CLLP, Bulgarian Academy of Sciences,
1113 Sofia, Bulgaria
<http://www.math.uh.edu>
<http://scicomp.math.uni-augsburg.de>

Figure 1 shows a classical example in structural optimization, namely the topology optimization of a cantilever consisting of a homogeneous, isotropic material with elasticity tensor $E = (E_{ijkl})$ occupying a fraction $\gamma|\Omega|$, $0 < \gamma < 1$, of a bounded domain $\Omega \subset \mathbb{R}^2$. Assuming that the cantilever is fixed on a part of its boundary and subject to volume and surface forces \mathbf{f} and \mathbf{t} , the issue is to distribute the material in such a way that the structure has maximal stiffness (minimal compliance). The state variable is the deformation \mathbf{u} of the cantilever, whereas the design variable is a density function $\rho \in K \subset \{\mu | \mu : \bar{\Omega} \rightarrow [0, 1]\}$ such that the class of admissible elasticity tensors is of the form $E(\rho) := \rho E$. The optimization problem can be stated as follows:

$$\inf_{\mathbf{u}, \rho} J(\mathbf{u}, \rho), \quad J(\mathbf{u}, \rho) := \int_{\Omega} \mathbf{f} \cdot \mathbf{u} \, dx + \int_{\Gamma_N} \mathbf{t} \cdot \mathbf{u} \, ds \quad (1)$$

where $\rho \in K$ and \mathbf{u} satisfy the equations of linear elasticity

$$-\operatorname{div} \boldsymbol{\sigma}(\mathbf{u}) = \mathbf{f} \quad \text{in } \Omega, \quad (2)$$

$$\mathbf{u} = 0 \quad \text{on } \Gamma_D, \quad (3)$$

$$\mathbf{n} \cdot \boldsymbol{\sigma}(\mathbf{u}) = \mathbf{t} \quad \text{on } \Gamma_N, \quad (4)$$

$$\mathbf{n} \cdot \boldsymbol{\sigma}(\mathbf{u}) = 0 \quad \text{elsewhere} \quad (5)$$

with Hooke's law $\boldsymbol{\sigma}(\mathbf{u}) = E(\rho)\boldsymbol{\varepsilon}(\mathbf{u})$ as the constitutive equation. Here, $\boldsymbol{\sigma}$ stands for the stress tensor and $\boldsymbol{\varepsilon}(\mathbf{u}) = 1/2(\nabla\mathbf{u} + (\nabla\mathbf{u})^T)$ refers to the linearized strain tensor. Moreover, $\rho \in K$ is subject to the equality constraint

$$\int_{\Omega} \rho \, dx = \gamma |\Omega|. \quad (6)$$

If we choose $\rho \in L^\infty(\bar{\Omega}; \{0, 1\})$, the resulting 0-1 optimization problem is ill-posed. As an appropriate relaxation, ρ is allowed to take all possible values between 0 and 1, i.e., $K := L^\infty(\bar{\Omega}; [0, 1])$.

Remark 1 In practice, the density function ρ is modified as follows: Firstly, to avoid problems with the loss of ellipticity, $0 < \rho_{\min} \ll 1$ is chosen as a lower bound. Secondly, to reduce the amount of "grey zones" in the design (regions where ρ attains intermediate values) the



Fig. 1 Topology optimization of a cantilever

extreme values 1 and ρ_{\min} are enforced. A possible way to do that is by the so-called SIMP-approach (simple isotropic material with penalization) where ρ is replaced by ρ^m with an appropriately chosen penalization parameter $m > 1$ (cf., e.g., [67]).

After discretization of the problem by conforming P2 elements for the state variable and conforming P1 elements for the design variable with respect to a simplicial triangulation of the computational domain (lower order finite elements give rise to unwanted checkerboard patterns in the design), the discretized optimization problem can be stated as a constrained nonlinear programming (NLP) problem:

$$\text{minimize } f(x_1, x_2) \quad (7a)$$

$$\text{over } (x_1, x_2) \in \mathbb{R}^{n_1} \times \mathbb{R}^{n_2},$$

$$\text{subject to: } h_1(x_1, x_2) := A(x_2)x_1 - b = 0, \quad (7b)$$

$$\text{subject to: } h_2(x_1, x_2) := Mx_2 - \gamma|\Omega| = 0, \quad (7c)$$

$$\rho_{\min} \leq x_{2,i} \leq 1, \quad 1 \leq i \leq n_2, \quad (7d)$$

where $x_1 \in \mathbb{R}^{n_1}$ and $x_2 \in \mathbb{R}^{n_2}$ stand for the discrete state and design variables, f represents the discretized objective functional, $A(x_2) \in \mathbb{R}^{n_1 \times n_1}$ and $b \in \mathbb{R}^{n_1}$ represent the stiffness matrix and the load vector of the discretized elasticity equations, and $M \in \mathbb{R}^{n_2 \times n_2}$ results from the discretization of the equality constraint (6).

As far as the solution of Eqs. 7a–7d is concerned, traditional techniques rely on what is called the alternating approach (cf., e.g., [1]): Given a design, the discretized state equations are numerically solved, followed by an update of the design variables based on an appropriate sensitivity analysis. This process is then continued until convergence. Recently, new and more efficient methods have been developed and implemented which use a so-called "all-at-once" strategy where the numerical solution of the discretized state equations is an integral part of the optimization routine (cf., e.g., [7, 8, 35, 39, 44, 53]). Typical representatives of this class of techniques are primal-dual Newton methods treating inequality constraints either by interior-point methods [35, 39, 44] or active set strategies [5, 29].

We emphasize that in this paper we follow the strategy "discretize first, then optimize". We remark that the alternative approach "optimize first, then discretize" can be realized as well, e.g., by considering interior-point methods in function space (see, for instance, [56–58, 61, 62]).

The paper is organized as follows: In Sect. 2, we consider primal-dual Newton interior-point methods focusing on the iterative solution of the primal-dual system arising from the application of Newton's method to the KKT conditions. We also discuss global

convergence issues by means of a hierarchy of merit functions combined with a suitable watchdog strategy. Then, in Sect. 3, we apply these methods to the structural optimization of biomimetic materials, namely biomorphic microcellular SiC ceramics, where the state equations are homogenized equations of linear elasticity and the design variables are geometric microstructural quantities. As an example of shape optimization in fluid mechanics, we consider the shape optimization of electrorheological shock absorbers. Here, the state equations are based on a regularized Bingham-type model, whereas the design parameters are the de Boor control points of a B-spline representation of the inlet and outlet boundaries of the electrorheological ducts of the fluid chamber. Finally, we address a topology optimization problem in high power electronics with the quasi-stationary limit of Maxwell's equations (eddy currents equations) as the state equations and the electric conductivity as the design variable.

2 Primal-dual Newton methods

We consider constrained NLP problems of the form

$$\text{minimize } f(x_1, x_2) \quad (8a)$$

$$\text{over } (x_1, x_2) \in \mathbb{R}^{n_1} \times \mathbb{R}^{n_2},$$

$$\text{subject to: } h(x_1, x_2) = 0, \quad (8b)$$

$$g(x_1, x_2) \geq 0, \quad (8c)$$

where $f : \mathbb{R}^{n_1} \times \mathbb{R}^{n_2} \rightarrow \mathbb{R}$ is the discretized objective functional depending on the discrete state variables $x_1 \in \mathbb{R}^{n_1}$ and design variables $x_2 \in \mathbb{R}^{n_2}$, (8b) with $h = (h_1, h_2)^T : \mathbb{R}^{n_1} \times \mathbb{R}^{n_2} \rightarrow \mathbb{R}^m$, $m \geq n_1$, comprises the discretized state equation $h_1 : \mathbb{R}^{n_1} \times \mathbb{R}^{n_2} \rightarrow \mathbb{R}^{n_1}$ and possibly further equality constraints $h_2 : \mathbb{R}^{n_1} \times \mathbb{R}^{n_2} \rightarrow \mathbb{R}^{m-n_1}$, whereas Eq. 8c with $g : \mathbb{R}^{n_1} \times \mathbb{R}^{n_2} \rightarrow \mathbb{R}^p$ represents inequality constraints on the state and design variables. If we define the feasible set \mathcal{F} according to

$$\mathcal{F} := \{(x_1, x_2) \mid h(x_1, x_2) = 0, \quad g(x_1, x_2) \geq 0\},$$

then the NLP 8a–8c can be written more concisely as

$$\min_{(x_1, x_2) \in \mathcal{F}} f(x_1, x_2). \quad (9)$$

The slack-variable formulation of the NLP is given by

$$\text{minimize } f(x_1, x_2) \quad (10a)$$

$$\text{over } (x_1, x_2, z) \in \mathbb{R}^{n_1} \times \mathbb{R}^{n_2} \times \mathbb{R}^p,$$

$$\text{subject to: } h(x_1, x_2) = 0, \quad (10b)$$

$$g(x_1, x_2) - z = 0, \quad (10c)$$

$$z \geq 0, \quad (10d)$$

where $z \in \mathbb{R}^p$ is called the vector of slack variables.

Classical algorithms for the numerical solution of Eqs. 8 rely either on the primal or on the dual formulation of the problem [6,23], whereas primal-dual methods take advantage of information provided by both the primal and dual variables that are treated as independent variables. They are based on the saddle point problem

$$\min_{(x_1, x_2) \in \mathbb{R}^{n_1} \times \mathbb{R}^{n_2}} \max_{(\lambda, \mu) \in \mathbb{R}^m \times \mathbb{R}_+^p} L(x_1, x_2, \lambda, \mu) \quad (11)$$

for the Lagrangian

$$\begin{aligned} L(x_1, x_2, \lambda, \mu) \\ := f(x_1, x_2) + \lambda^T h(x_1, x_2) - \mu^T g(x_1, x_2), \end{aligned} \quad (12)$$

where $\lambda \in \mathbb{R}^m$ and $\mu \in \mathbb{R}_+^p$ are the Lagrange multipliers (dual variables) associated with the equality and inequality constraints.

The KKT conditions give rise to the nonlinear system

$$\begin{bmatrix} \nabla f(x) + \nabla h(x)\lambda + \nabla g(x)\mu \\ h(x) \\ g(x) - z \\ D_z D_\mu e \end{bmatrix} = 0,$$

where $D_z = \text{diag}(z_1, \dots, z_p)$, $D_\mu = \text{diag}(\mu_1, \dots, \mu_p)$ and $e = (1, \dots, 1)^T$.

The Newton aspect is to apply Newton's method to the Karush–Kuhn–Tucker (KKT) conditions associated with the primal-dual formulation. This means that each Newton step requires the solution of a linear algebraic system representing the optimality conditions of a related quadratic programming (QP) problem. Hence, primal-dual Newton methods can be interpreted in the framework of sequential quadratic programming (SQP) which is the most successful method for solving constrained nonlinear optimization problems [9,47].

As far as the appropriate treatment of the inequality constraints is concerned, a local optimum can be approximated from within the feasible set, which is the idea behind interior-point methods [20,64–66], or by using active set strategies where the iterates are not restricted to feasibility (cf., e.g., [5,29] for recent work in the context of constrained optimal control problems).

2.1 Interior-point methods

The so-called interior-point revolution in continuous optimization started in the 1980s of the last century with Karmarkar's polynomial-time linear programming algorithm [43]. It was immediately found [22] that there is a close relationship to barrier functions which had been used long time before for inequality constrained NLP problems. Nowadays, interior-point methods are

well-established tools for constrained nonlinear optimization problems (cf., e.g., [20, 64–66] and the references therein).

Barrier methods are used to transform constrained problems to unconstrained ones and typically give rise to parametrized families of approximate subproblems whose solutions converge asymptotically to the exact solution along centered paths tracing smooth trajectories with algebraic and geometric properties (for path-following continuation methods see, e.g., [16]). They are related to the slack variable formulation 10 of the NLP problem.

Here, we focus on the coupling of the inequality constraints 8c by classical logarithmic barrier functions

$$B^{(\beta)}(x_1, x_2) := f(x_1, x_2) - \beta \sum_{i=1}^p \log(g_i(x_1, x_2)), \quad (13)$$

where $\beta > 0$ stands for the barrier parameter [18, 20, 64]. This leads to the consideration of the following parametrized family of minimization subproblems

$$\text{minimize } B^{(\beta)}(x_1, x_2) \quad (14a)$$

$$\text{over } (x_1, x_2) \in \mathbb{R}^{n_1} \times \mathbb{R}^{n_2},$$

$$\text{subject to: } h(x_1, x_2) = 0. \quad (14b)$$

Theorem 1 ([18]) Assume that the NLP 8a–8c satisfies the linear independence constraint qualification and the first and second order optimality conditions as well as strict complementarity. Then, for sufficiently small $\beta > 0$ there exist local minima $(x_1^{(\beta)}, x_2^{(\beta)})$ of Eqs. (14a), and (14b) which converge to an isolated local minimum of Eqs. 8a–8c as $\beta \rightarrow 0$.

The equality constraint 14b is taken care of by a Lagrangian multiplier $\lambda = (\lambda_1, \lambda_2)^T, \lambda_1 \in \mathbb{R}^{n_1}, \lambda_2 \in \mathbb{R}^{m-n_1}$, so that we associate with Eqs.(14a) and (14b) the Lagrangian

$$L^{(\beta)}(x_1, x_2, \lambda) := B^{(\beta)}(x_1, x_2) + \lambda^T h(x_1, x_2) \quad (15)$$

and consider the saddle point problem

$$\min_{(x_1, x_2) \in \mathbb{R}^{n_1} \times \mathbb{R}^{n_2}} \max_{\lambda \in \mathbb{R}^m} L^{(\beta)}(x_1, x_2, \lambda). \quad (16)$$

The KKT-conditions for Eq. 16 are given by

$$\begin{aligned} \nabla_{x_1} L^{(\beta)}(x_1, x_2, \lambda) &= \nabla_{x_1} f(x_1, x_2) \\ &+ \nabla_{x_1} h(x_1, x_2) \lambda - \sum_{i=1}^p \frac{\beta}{g_i(x_1, x_2)} \nabla_{x_1} g_i(x_1, x_2) = 0, \\ \nabla_{x_2} L^{(\beta)}(x_1, x_2, \lambda) &= \nabla_{x_2} f(x_1, x_2) \\ &+ \nabla_{x_2} h(x_1, x_2) \lambda - \sum_{i=1}^p \frac{\beta}{g_i(x_1, x_2)} \nabla_{x_2} g_i(x_1, x_2) = 0, \\ \nabla_{\lambda} L^{(\beta)}(x_1, x_2, \lambda) &= h(x_1, x_2) = 0. \end{aligned}$$

The Hessian of the Lagrangian $L^{(\beta)}$ is ill-conditioned as $\beta \rightarrow 0$. We introduce the slack variable $z^{(\beta)} \in \mathbb{R}^p$ according to

$$z_i^{(\beta)} := \frac{\beta}{g_i(x_1, x_2)}, \quad 1 \leq i \leq p, \quad (17)$$

which is referred to as approximate complementarity, since the following result holds true:

Corollary 1 *Suppose that the conditions of Theorem 1 are satisfied. Then, for $\beta \rightarrow 0$ the approximate complementarity $z^{(\beta)}$ converges to the optimal $z \in \mathbb{R}_+^p$ in the slack-variable formulation 10a–10d of the NLP.*

For notational convenience, in the sequel we will drop the upper index β for the approximate complementarity.

If we use Eq. 17 in the KKT conditions and apply Newton's method with respect to $\varphi = (x_1, x_2, \lambda, z)$, we arrive at the primal-dual system

$$K \delta_\varphi = -F^{(\beta)}(\varphi) \quad (18)$$

for the Newton increments $\delta_\varphi := (\delta_{x_1}, \delta_{x_2}, \delta_\lambda, \delta_z)^T$, where the right-hand side is the residual with respect to the KKT conditions and the primal-dual matrix K is given by

$$K = \begin{pmatrix} \nabla_{x_1 x_2}^2 L^{(\beta)} & \nabla_{x_1 x_2}^2 L^{(\beta)} & (\nabla_{x_1} h)^T & -(\nabla_{x_1} g)^T \\ \nabla_{x_2 x_1}^2 L^{(\beta)} & \nabla_{x_2 x_2}^2 L^{(\beta)} & (\nabla_{x_2} h)^T & -(\nabla_{x_2} g)^T \\ \nabla_{x_1} h & \nabla_{x_2} h & 0 & 0 \\ \nabla_{x_1} g & \nabla_{x_2} g & 0 & D_z^{-1} D_g \end{pmatrix}$$

with $D_g := \text{diag}(g_i(x_1, x_2))_{i=1}^p$ and $D_z := \text{diag}(z_i)_{i=1}^p$.

Since D_g, D_z are diagonal matrices, it is easy to perform block Gauss elimination of the approximate complementarity z which leads to the condensed primal-dual system in $\delta_{\varphi^{(C)}} = (\delta_{x_1}, \delta_{x_2}, \delta_\lambda)^T$

$$K^{(C)} \delta_{\varphi^{(C)}} = -F^{(C)}(\varphi^{(C)}) \quad (19)$$

with the condensed primal-dual matrix

$$K^{(C)} = \begin{pmatrix} \tilde{\nabla}_{x_1 x_1}^2 L^{(\beta)} & \tilde{\nabla}_{x_1 x_2}^2 L^{(\beta)} & (\nabla_{x_1} h)^T \\ \tilde{\nabla}_{x_2 x_1}^2 L^{(\beta)} & \tilde{\nabla}_{x_2 x_2}^2 L^{(\beta)} & (\nabla_{x_2} h)^T \\ \nabla_{x_1} h & \nabla_{x_2} h & 0 \end{pmatrix}. \quad (20)$$

Note that for $1 \leq i, j \leq 2$

$$\tilde{\nabla}_{x_i x_j}^2 L^{(\beta)} = \nabla_{x_i x_j}^2 L^{(\beta)} + (\nabla_{x_i} g)^T D_g^{-1} D_z \nabla_{x_j} g,$$

and that the right-hand side in Eq. 19 is given by

$$F_{x_i}^{(C)}(\varphi^{(C)}) = \nabla_{x_i} f + \nabla_{x_i} h - \beta (\nabla_{x_i} g)^T D_g^{-1} e,$$

$$F_{\lambda}^{(C)}(\varphi^{(C)}) = h, \quad \text{where } e = (1, \dots, 1)^T \in \mathbb{R}^p.$$

For the numerical solution of the condensed primal-dual system 19 we will take advantage of its structural properties. Observing $h = (h_1, h_2)^T$, the condensed primal-dual matrix 20 has the following 2×2 block structure

$$K^{(C)} = \begin{pmatrix} \tilde{\nabla}_{x_1 x_1}^2 L^{(\beta)} & \tilde{\nabla}_{x_1 x_2}^2 L^{(\beta)} & | & (\nabla_{x_1} h_1)^T & (\nabla_{x_1} h_2)^T \\ \tilde{\nabla}_{x_2 x_1}^2 L^{(\beta)} & \tilde{\nabla}_{x_2 x_2}^2 L^{(\beta)} & | & (\nabla_{x_2} h_1)^T & (\nabla_{x_2} h_2)^T \\ \hline \nabla_{x_1} h_1 & \nabla_{x_2} h_1 & | & 0 & 0 \\ \nabla_{x_1} h_2 & \nabla_{x_2} h_2 & | & 0 & 0 \end{pmatrix}.$$

We note that Eq. (19) resembles the optimality system of an equality constrained QP problem. As far as the direct solution of such systems is concerned, there are basically two techniques: the range space method applies when the first diagonal block in $K^{(C)}$ is easily invertible, whereas the null space approach is used otherwise providing a basis for the kernel of the matrix associated with the equality constraints [23]. These methodologies can be adopted to the iterative solution of Eq. 19 as well. We note that the range space is not appropriate in the situation at hand. Observing that $\nabla_{x_1} h_1$ is the Jacobian of the discretized state equations and assuming that an efficient iterative solver for its solution is available, we will follow the null space method and regroup the unknowns according to

$$y_1 := (x_1, \lambda_1)^T, \quad y_2 := (x_2, \lambda_2)^T. \quad (21)$$

This goes along with a rearrangement of the primal-dual matrix $K^{(C)}$ by interchanging the second and third rows and columns. We thus arrive at the following linear system

$$A \delta_y = \begin{pmatrix} A_{11} & A_{12} \\ A_{21} & A_{22} \end{pmatrix} \begin{pmatrix} \delta_{y_1} \\ \delta_{y_2} \end{pmatrix} = - \begin{pmatrix} b_1 \\ b_2 \end{pmatrix} \quad (22)$$

with the 2×2 block matrices $A_{ij}, 1 \leq i, j \leq 2$,

$$\begin{aligned} A_{11} &= \begin{pmatrix} \tilde{\nabla}_{x_1 x_1}^2 L^{(\beta)} & (\nabla_{x_1} h_1)^T \\ \nabla_{x_1} h_1 & 0 \end{pmatrix}, \\ A_{12} &= \begin{pmatrix} \tilde{\nabla}_{x_1 x_2}^2 L^{(\beta)} & (\nabla_{x_1} h_2)^T \\ \nabla_{x_2} h_1 & 0 \end{pmatrix}, \\ A_{21} &= \begin{pmatrix} \tilde{\nabla}_{x_2 x_1}^2 L^{(\beta)} & (\nabla_{x_2} h_1)^T \\ \nabla_{x_1} h_2 & 0 \end{pmatrix}, \\ A_{22} &= \begin{pmatrix} \tilde{\nabla}_{x_2 x_2}^2 L^{(\beta)} & (\nabla_{x_2} h_2)^T \\ \nabla_{x_2} h_2 & 0 \end{pmatrix}, \end{aligned}$$

and the right-hand side b given by

$$\begin{aligned} b_1 &= (\nabla_{x_1} f + \nabla_{x_1} h_1 + \nabla_{x_1} h_2 - \beta (\nabla_{x_1} g)^T D_g^{-1} e, h_1)^T, \\ b_2 &= (\nabla_{x_2} f + \nabla_{x_2} h_1 + \nabla_{x_2} h_2 - \beta (\nabla_{x_2} g)^T D_g^{-1} e, h_2)^T. \end{aligned}$$

For the iterative solution of Eq. 22 we use right-transforming iterations with the right transform

$$T_R := \begin{pmatrix} I & -\hat{A}_{11}^{-1} A_{12} \\ 0 & I \end{pmatrix}, \quad (23)$$

where

$$\hat{A}_{11} := \begin{pmatrix} \tilde{\nabla}_{x_1 x_1}^2 L^{(\beta)} & (\hat{\nabla}_{x_1} h_1)^T \\ \hat{\nabla}_{x_1} h_1 & 0 \end{pmatrix}$$

and $\hat{\nabla}_{x_1} h_1$ is an approximation of the Jacobian $\nabla_{x_1} h_1$ in the sense that $(\hat{\nabla}_{x_1} h_1)^{-1}$ has to be interpreted as the application of the available iterative solver for the linearized discretized state equations. The right transform 23 induces the splitting

$$AT_R := M - N, \quad (24)$$

where

$$\begin{aligned} M &= \begin{pmatrix} \hat{A}_{11} & 0 \\ A_{21} & S \end{pmatrix}, \quad S := A_{22} - A_{21} \hat{A}_{11}^{-1} A_{12}, \\ N &= \begin{pmatrix} (I - A_{11} \hat{A}_{11}^{-1}) \hat{A}_{11} & (I - A_{11} \hat{A}_{11}^{-1}) A_{12} \\ 0 & 0 \end{pmatrix}. \end{aligned}$$

Note that $(\hat{\nabla}_{x_1} h_1)^{-1} \nabla_{x_1} h_1 \sim I$ implies $\hat{A}_{11}^{-1} A_{11} \sim I$, and hence, $N \sim 0$.

Now, given an iterate $\delta_y^{(0)}$, the right transforming iteration is as follows:

$$\delta_y^{(v+1)} = (I - T_R M^{-1} A) \delta_y^{(v)} - T_R M^{-1} b, \quad v \geq 0. \quad (25)$$

The implementation of Eq. 25 requires the solution of the block system

$$M v^{(v+1)} = r^{(v)} := b + a \delta_y^{(v)}.$$

We then compute $w^{(v+1)} = T_R v^{(v+1)}$ according to

$$w_1^{(v+1)} = v_1^{(v+1)} - \hat{A}_{11}^{-1} A_{12} v_2^{(v+1)}, \quad w_2^{(v+1)} = v_2^{(v+1)},$$

and finally get the new iterate by

$$\delta_y^{(v+1)} = \delta_y^{(v)} - w^{(v+1)}.$$

Stopping the iteration at a prescribed accuracy, the last iterate is accepted as the Newton increment δ_y . Observing Eq. 18, the increment δ_z in the approximate complementarity is obtained according to

$$\delta_z = z - [\beta e + D_z (\nabla_{x_1} g \delta_{x_1} + \nabla_{x_2} g \delta_{x_2})].$$

Remark 2 We note that right transforming iterations have been systematically studied in the framework of multilevel iterative solvers for PDEs [63]. For the iterative solution of primal-dual systems in PDE constrained optimization problems, they have been used for the first time in [44].

The efficiency of primal-dual interior point methods can be strongly influenced by an appropriate steplength selection (line-search) [47]. Here, we use two different step-lengths s_1 for the primal variables $x = (x_1, x_2)^T$ and s_2 both for the dual variable λ and the approximate complementarity z :

$$x \mapsto x + s_1 \delta_x, \quad \begin{cases} \lambda \mapsto \lambda + s_2 \delta_\lambda \\ z \mapsto z + s_2 \delta_z \end{cases}. \quad (26)$$

The steplengths $s_i, 1 \leq i \leq 2$, are chosen such that feasibility of the iterates is maintained:

$$s_i := \min(1, \tau, \gamma_i), \quad 1 \leq i \leq 2,$$

where

$$\tau := 1 - \min(\varepsilon, C\beta^2)$$

with problem dependent parameters $0 < \varepsilon \ll 1, C > 0$, and $\gamma_i, 1 \leq i \leq 2$, chosen according to

$$\gamma_1 := \max \{t \mid g(x) + t \nabla_x g(x) \delta_x \geq 0\},$$

$$\gamma_2 := \max \{t \mid z + t \delta_z \geq 0\}.$$

Remark 3 In practice, an additional update of the dual variables is performed involving the solution of a least-squares problem. We refer to [35] for details.

Remark 4 We note that interior-point methods for non-linear optimization problems based on a trust-region approach have been considered in [15].

In SQP methods, global convergence can be achieved by using appropriately chosen merit functions for convergence monitoring (cf., e.g., [9]). Relying only on the widely used ℓ_2 -norm of the residual with respect to the KKT conditions is not appropriate for discretized structural optimization problems, since it does not distinguish between critical points and one might end up with a saddle point instead of a local minimum. A better choice is a hierarchy of two merit functions [21] combined with a watchdog strategy originally proposed in [12]. The primary merit function is chosen as the augmented Lagrangian

$$\begin{aligned} M^{(\beta)}(x_1, x_2, \lambda, \sigma) \\ := f(x_1, x_2) - \beta \sum_{i=1}^p \log(g_i(x_1, x_2)) \\ + \lambda^T h(x) + \frac{\sigma}{2} h(x)^T h(x), \end{aligned} \quad (27)$$

whereas the standard ℓ_2 -norm of the residual with respect to the KKT conditions serves as the secondary merit function

$$\mathcal{F}(x_1, x_2, \lambda, z) := \|F^{(\beta)}(x_1, x_2, \lambda, z)\|_2. \quad (28)$$

The watchdog strategy works as follows: The line-search counter $lsteps$ and the watchdog counter $watchsteps$ are set to zero. The computed steplengths are accepted, if a decrease of the primary merit function is realized. Otherwise, the secondary merit function is checked. If it has decreased, the steplengths are accepted and the watchdog counter is increased by one ($watchsteps \leftarrow watchsteps + 1$). If not, the steplengths $s_i, 1 \leq i \leq 2$, are damped according to $s_i \leftarrow s_i/2$ and the line-search counter $lsteps$ is increased by one ($lsteps \leftarrow lsteps + 1$). However, if a total number of $watchmax$ watchdog iterations has occurred without a reduction of the primary merit function, we return to the initial iterates and choose the penalty parameter σ large enough to guarantee a decrease of the primary merit function. After each steplength iteration, the barrier parameter β is updated as well by means of the following heuristic rule (cf. [21]):

If $lsteps < lmax_1$ or β remained unchanged for $lmax_2$ iterations, in case $\mathcal{F}(x_1, x_2, \lambda, z) < 10\beta$ we set

$$\begin{cases} \beta \leftarrow 10\beta^2 \\ \beta \leftarrow \beta/10 \end{cases} \quad \text{if} \quad \begin{cases} \beta < 10^{-4} \\ \text{otherwise} \end{cases},$$

whereas

$$\beta \leftarrow 0.8\beta$$

is chosen for $\mathcal{F}(x_1, x_2, \lambda, z) \geq 10\beta$.

Otherwise, β remains unchanged. (Typical values for $lmax_1$ and $lmax_2$ are $lmax_1 = 3$ and $lmax_2 = 10$).

3 Structural optimization in materials science

3.1 Structural optimization of microcellular biomorphic ceramics

Biomimetics is a discipline in materials science where engineers mimic or use the pronounced functionality of biological objects to design technologically relevant devices and systems of higher performance than those produced by conventional manufactural techniques. A particular area in biomimetics is the production of mechanically robust, highly porous ceramics from naturally grown wood by biotemplating [25,26]. Biotemplating is a two-step process (cf. Fig. 2): in the first step, wooden specimen are pyrolyzed at high temperatures resulting in a graphite-like carbon preform while preserving the high porosity of the original specimen cf. Fig. 3 (left).

In the second step, the carbon preform is infiltrated by liquid or gaseous silicon (Si) or titanium (Ti) which reacts with the carbon and results in the final microcellular SiC or TiC ceramics [cf. Fig. 3 (right)]. Often, the

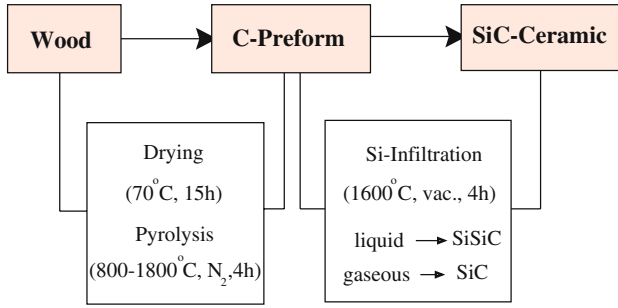


Fig. 2 Two-step processing of wooden specimen

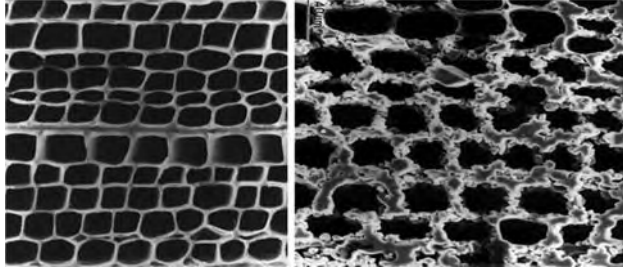


Fig. 3 Pyrolyzed pine (left) and Si-infiltrated specimen (right)

inner walls are additionally coated by a thin layer of oxide to enhance the densification of the structure.

Due to its excellent mechanical properties (cf. Table 1; see also [59]), such ceramics are used as filters in chemical processing, as high performance brakes in vehicles, or as implant materials in biomedical applications [54, 60, 68].

We assume the workpiece of macroscopic length L to consist of periodically distributed constituents with a periodicity cell Y of characteristic microscopic length ℓ consisting of an interior void (V) surrounded by layers of silicon carbide (SiC) resp. titanium carbide (TiC) and carbon (C) (cf. Fig. 4).

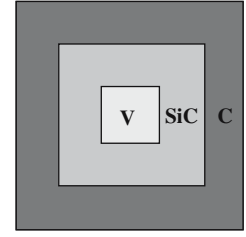
Assuming linear elasticity and denoting by \mathbf{u} the displacement vector, the stress tensor $\boldsymbol{\sigma}$ is related to the linearized strain tensor $\mathbf{e} = 1/2(\nabla\mathbf{u} + (\nabla\mathbf{u})^T)$ by Hooke's

Table 1 Mechanical properties of microstructured biomorphic SiC ceramics

	Material	ρ (g/cm ³)	β (MPa)	κ (vol)
C_B -Template	C_B	0.39	7	76
Si-melt (1600° C)	SiSiC	2.22	130	11
MTS (1600° C)	SiC _{MTS}	0.8–1.0	210	60
Si-vapor (1600° C)	SiC _{Si}	1.0	13	71
SiO-vapor (1600° C)	SiC _{SiO}	0.7	8	78

density ρ , bending strength β , and porosity κ

Fig. 4 Periodicity cell



law $\boldsymbol{\sigma} = E(X)\mathbf{e}$, where $E(X) = (E_{ijkl}(X))$ stands for the elasticity tensor whose components attain different values in the regions V, SiC (resp. TiC), and C.

Introducing $x := X/L$ and $y := X/\ell$ as the macroscopic and microscopic variables and $\varepsilon := \ell/L$ as the scale parameter, homogenization based on the standard double scale asymptotic expansion results in the homogenized elasticity tensor $E^H = (E_{ijkl}^H)$ whose components are given by

$$E_{ijkl}^H = \frac{1}{|Y|} \int_Y \left(E_{ijkl}(y) - E_{ijpq}(y) \frac{\partial \xi_p^{k\ell}}{\partial y_q} \right) dy. \quad (29)$$

The tensor $\boldsymbol{\xi} = (\xi_p^{k\ell})$ with periodic components $\xi_p^{k\ell} \in H_{\text{per}}^1(Y)$ has to be computed via the solution of the elasticity problems

$$\text{div}_y(E(y) - E(y)\mathbf{e}_y(\boldsymbol{\xi}^{k\ell})) = 0. \quad (30)$$

We note that explicit formulas for the homogenized elasticity tensor are only available in case of laminated or checkerboard structures (cf., e.g., [1, 3, 4]). Therefore, Eq. 30 has to be solved numerically which has been done by using continuous, piecewise linear finite elements with respect to adaptively generated locally quasi-uniform and shape regular simplicial triangulations of the periodicity cell Y . The discretized problems have been solved by algebraic multigrid and the mesh adaptivity has been realized by means of a Zienkiewicz-Zhu type a posteriori error estimator [42] (cf. Fig. 5).

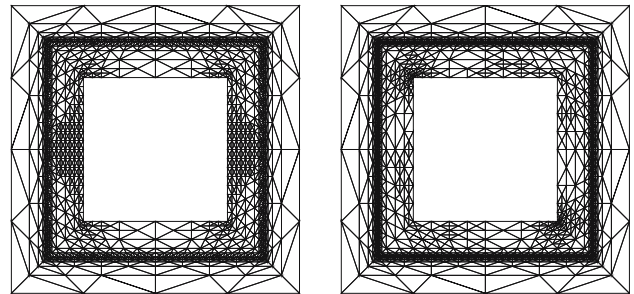
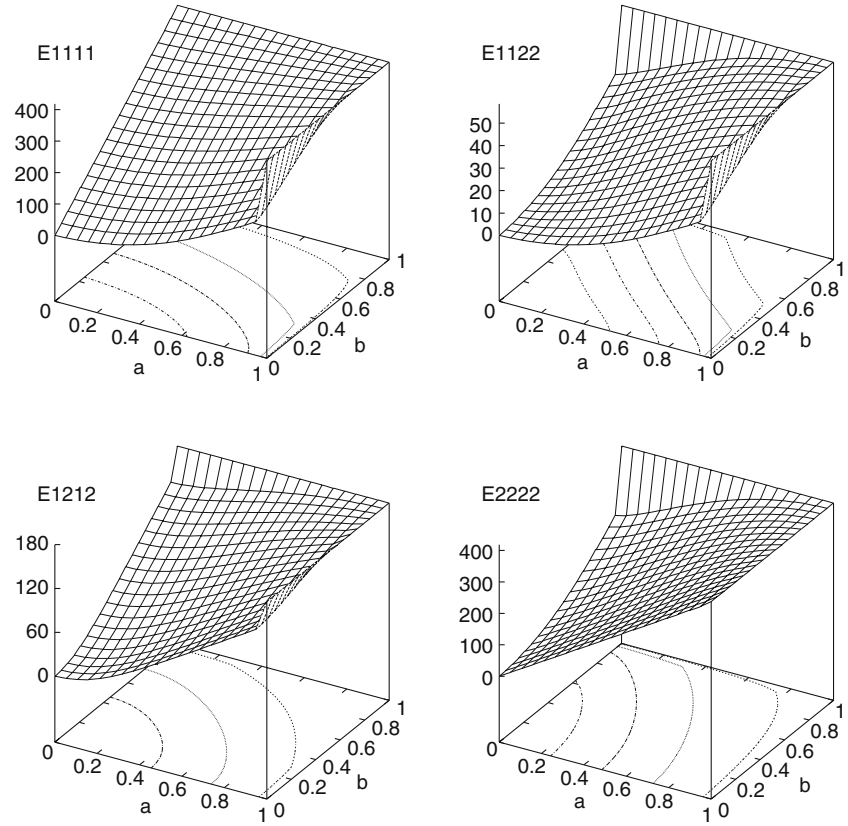


Fig. 5 Adaptively generated FE grids in the computation of the homogenized elasticity coefficients E_{1111}^H (9 refinement levels; left) and E_{1212}^H (10 refinement levels; right)

Fig. 6 Dependence of the homogenized elasticity tensor on the width and length of the SiC layer



The homogenized elasticity tensor E^H depends on the lengths and widths of the different layers as well as on the angle θ of orientation of the microcell Y with respect to the reference frame which serve as the design variables $\alpha = (\alpha_1, \dots, \alpha_m)$ in the structural optimization. An explicit formula is only available for the dependence on θ . Consequently, the dependence on the other design variables has been provided numerically by multivariate interpolation using B-splines with respect to a uniform grid of the space of the design parameters (cf. Fig. 6 for the dependence on the length of the SiC-layer and Fig. 7 for the dependence on the angle of orientation).

The choice of the objective functional depends on the application. Various mechanical merit functions can be chosen including maximal stiffness and bending strength. The structural optimization problem can then be stated as follows:

$$\inf_{\mathbf{u}, \alpha} J(\mathbf{u}, \alpha) \quad (31)$$

subject to the state equations

$$-\operatorname{div} \boldsymbol{\sigma}(\mathbf{u}) = \mathbf{f} \quad \text{in } \Omega, \quad (32)$$

$$\mathbf{u} = 0 \quad \text{on } \Gamma_D, \quad (33)$$

$$\mathbf{n} \cdot \boldsymbol{\sigma}(\mathbf{u}) = \mathbf{t} \quad \text{on } \Gamma_N, \quad (34)$$

$$\mathbf{n} \cdot \boldsymbol{\sigma}(\mathbf{u}) = 0 \quad \text{elsewhere}, \quad (35)$$

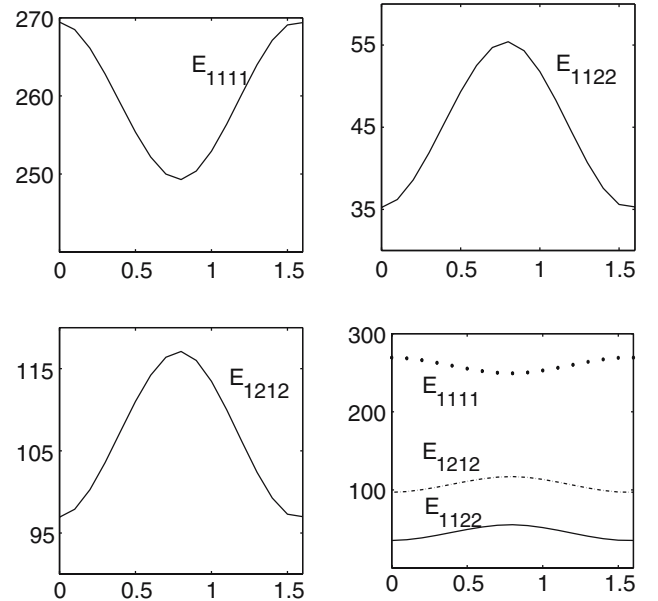


Fig. 7 Dependence of the homogenized elasticity tensor on the angle of orientation of the cell walls with respect to the reference frame

where the stress tensor $\boldsymbol{\sigma}$ is related to the strain tensor \mathbf{e} by Hooke's law

$$\boldsymbol{\sigma}(\mathbf{u}) = E^H(\alpha) \mathbf{e}(\mathbf{u}) \quad (36)$$

with the homogenized elasticity tensor $E^H(\alpha)$.

Table 2 Convergence history of the primal-dual Newton interior-point method (biomorphic SiC ceramics, minimum compliance)

N_E	iter	α	β	$M^{(\beta)}$	\mathcal{F}
160	19	8.1E-16	2.5E-25	0.840	2.9E-8
640	14	7.7E-10	9.1E-17	0.018	2.7E-5
1,048	11	4.6E-14	3.1E-22	0.53	4.5E-7
8704	11	3.7E-13	6.6E-21	0.29	1.1E-6
14,848	12	5.3E-13	8.3E-19	0.81	1.7E-6

We further impose the total mass in terms of the homogenized density $\rho(\alpha)$

$$\int_{\Omega} \rho(\alpha) dx = C \quad (37)$$

The design variables are assumed to satisfy the box constraints

$$\alpha_i^{\min} \leq \alpha_i \leq \alpha_i^{\max}, \quad 1 \leq i \leq m. \quad (38)$$

The structural optimization problem has been discretized by conforming P1 finite elements with respect to a simplicial triangulation of the computational domain and solved by the primal-dual Newton interior-point method. The numerical solution of the discretized state equations within the optimization cycle has been taken care of by the Algebraic Multi-Grid (AMG) method as a “plug-in” solver (see [51] for details).

Table 2 contains the convergence history of the primal-dual Newton interior-point method for the minimum compliance as the objective functional and no constraint on the total mass. In the table, N_E is the number of elements used in the finite element discretization of the homogenized model, “iter” stands for the number of iterations until convergence, α is the optimal length of the C-layer, β is the last value of the barrier parameter, and $M^{(\beta)}$, \mathcal{F} are the final values of the primary and secondary merit functions. For further results we refer to [31–33, 36, 40].

3.2 Shape optimization of electrorheological shock absorbers

Electrorheological fluids are concentrated suspensions of small electrically polarizable particles with diameters in the range of micrometers dissolved in nonconducting silicon oils. The rheological effect is based on the fact that under the influence of an outer electric field the particles form chains along the field lines and then aggregate to form larger and larger columns. The impact on the macroscopic scale consists in a rapid change of the rheological properties which happens within a few milliseconds. The viscosity increases in the direction

orthogonal to the electric field such that the character of the fluid changes from liquid to almost solid. Under the action of large stresses, depending on the electric field strength (field dependent yield stress), the columnar structures break such that the viscosity decreases and the fluid behaves less anisotropic. The process is reversible, i.e., the viscosity decreases with decreasing field strength and the fluid behaves again like a Newtonian fluid for vanishing outer electric field.

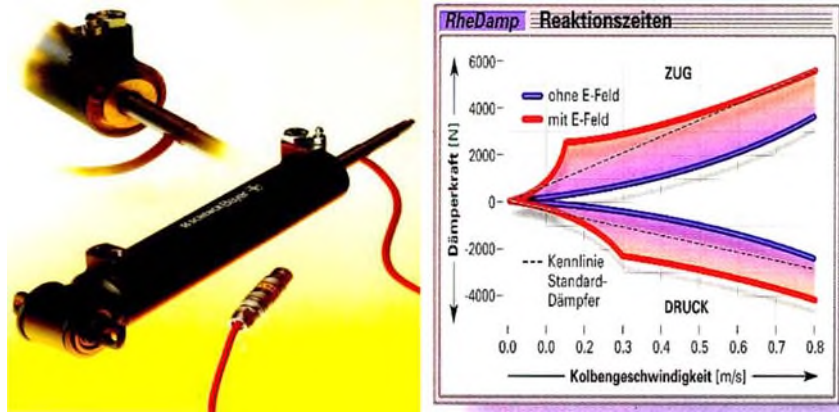
Therefore, electrorheological fluids are used in all technological processes where a controlled power transmission plays a significant role. The field of applications ranges from automotive shock absorbers and actuators in hydraulic systems to tactile devices for virtual reality [19].

In the sequel, we shall be concerned with the optimization of the shape of the walls of an ERF shock absorber [cf. Fig. 8 (left)] in a vicinity of the inlet and outlet boundary of the ERF transfer ducts. A schematic diagram of such a shock absorber is shown in Fig. 9 (left). The absorber contains two chambers filled with an ERF, a piston with two transfer ducts connecting the chambers, and a third gas-filled chamber separated from the others by a floating piston. The inner walls of the transfer ducts serve as electrodes and counter-electrodes, respectively. The electrodes are connected with an outer power source by a high voltage lead within the piston rod. As the piston moves, the fluid passes through the ducts from one chamber to the other. In the compression stage, the piston moves downwards and the ERF is streaming from the lower into the upper chamber, whereas in the rebound stage, the piston is pulled upwards and the ERF flow is in the opposite direction.

In contrast to conventional shock absorbers, where the fluid chambers are filled with hydraulic oils, both in the compression and in the rebound stage, ERF shock absorbers have a much wider characteristics [damper force as a function of the velocity of the piston; cf. Fig. 8 (right)]. Therefore, ERF shock absorbers offer the best compromise between safety and comfort for a wide spectrum of road conditions.

The performance of the shock absorber does not only depend on the applied voltage and the velocity of the piston, but also on the geometry of the device. In particular, the geometry of the inlet and outlet boundaries of the ducts plays a decisive role. In extreme cases, cavitation due to high pressure variations may occur which negatively affects the damper characteristics. Therefore, given a prescribed pressure profile p_d , the optimization issue is to design the geometry in such a way that pressure variations are minimized. Due to axisymmetry, the computational domain Ω reduces to the right part of the fluid chamber. The inlet and outlet boundaries

Fig. 8 Electrorheological shock absorber (left) and its characteristics (right); (Courtesy of Fluidicon GmbH)



are represented by B-splines using the de Boor control points $\alpha = (\alpha_1, \dots, \alpha_m)$ as design variables [cf. Fig. 9 (right)]. Consequently, the computational domain depends on the choice of the design variables, i.e., $\Omega = \Omega(\alpha)$.

In the stationary case, the fluid flow is described by the equations

$$-\nabla \cdot \sigma(\mathbf{u}) = \mathbf{f} \quad \text{in } \Omega(\alpha), \quad (39)$$

$$\nabla \cdot \mathbf{u} = 0 \quad \text{in } \Omega(\alpha) \quad (40)$$

along with appropriate boundary conditions. Here, $\mathbf{u} = (u_1, u_2)$ is the velocity vector, σ refers to the stress tensor and \mathbf{f} describes exterior forces acting on the fluid. The stress tensor σ is related to the rate of deformation tensor $\mathbf{D}(\mathbf{u})$ with $(\mathbf{D}(\mathbf{u}))_{ij} := (\partial u_i / \partial x_j + \partial u_j / \partial x_i) / 2$, $1 \leq i, j \leq 2$, by a constitutive equation where the electric field \mathbf{E} enters as a parameter. Most constitutive equations are of extended Bingham fluid type [17, 49] and use some sort of power law dependence [52]. Here, we use a constitutive equation developed in [34]

$$\sigma = -p \mathbf{I} + 2 \varphi(I(\mathbf{u}), |\mathbf{E}|, \mu(\mathbf{u}, \mathbf{E})) \mathbf{D}(\mathbf{u}), \quad (41)$$

where φ is a viscosity function depending on the shear rate $I(\mathbf{u})$, the electric field strength $|\mathbf{E}|$, and the angle $\mu(\mathbf{u}, \mathbf{E})$ between the velocity field \mathbf{u} and the electric field \mathbf{E} . In particular, the viscosity function φ is assumed to be of the form

$$\begin{aligned} \varphi(I(\mathbf{u}), |\mathbf{E}|, \mu(\mathbf{u}, \mathbf{E})) \\ = b(|\mathbf{E}|, \mu(\mathbf{u}, \mathbf{E})) (\varepsilon + I(\mathbf{u}))^{-1/2} \\ + \psi(I(\mathbf{u}), |\mathbf{E}|, \mu(\mathbf{u}, \mathbf{E})), \end{aligned} \quad (42)$$

where $\varepsilon > 0$ is a regularization parameter. In practice, the functions b and ψ are approximated by splines fitted to rheometrical data obtained for different electric field strengths (cf. Fig. 10).

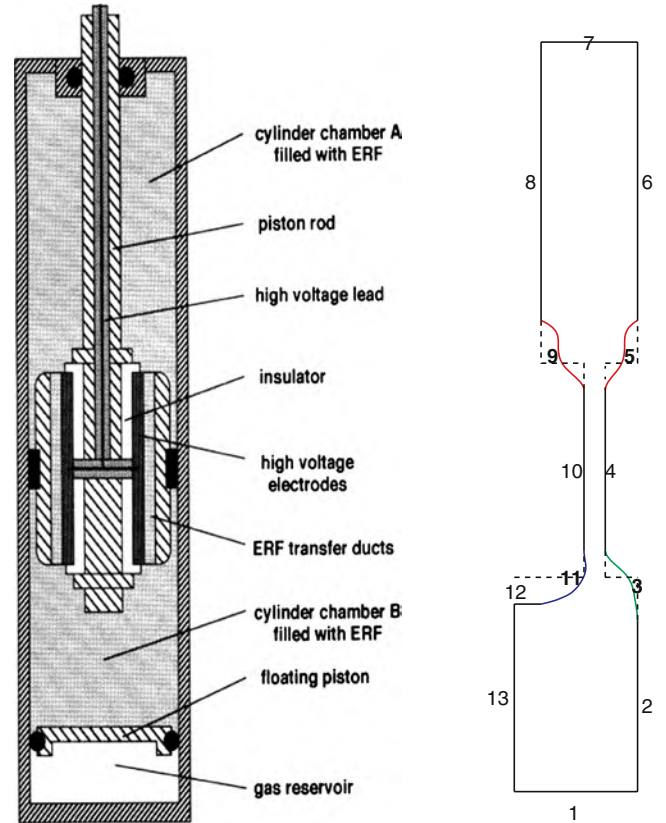


Fig. 9 Electrorheological shock absorber: schematic diagram (left) and B-Spline representation of the inlet and outlet boundaries of the right part of the fluid chamber (right)

The shape optimization problem can be stated as follows:

$$\inf_{(\mathbf{u}, p, \alpha)} J(\mathbf{u}, p, \alpha), \quad J(\mathbf{u}, p, \alpha) := \int_{\Omega(\alpha)} |\nabla p - \nabla p_d|^2 dx \quad (43)$$

subject to the state equations 39 and 40 and the inequality constraints

$$\alpha_i^{\min} \leq \alpha_i \leq \alpha_i^{\max}, \quad 1 \leq i \leq m \quad (44)$$

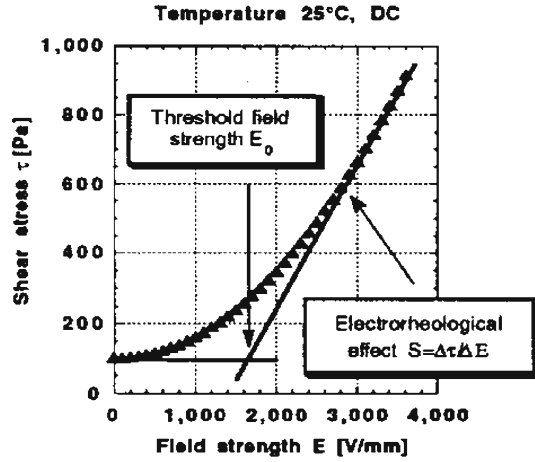


Fig. 10 Dependence of the shear stress on the electric field strength (Rheobay TP AI 3565, polyurethane); from [2]

on the design variables which are motivated by technological constraints on the shape of the inlet and outlet boundaries.

The finite element discretization of the optimization problem is based on the variational formulation of the state equations 39 and 40 which is given by

$$\left\langle \frac{\partial F_\varepsilon}{\partial \mathbf{w}}(\mathbf{u}, \mathbf{u}), \mathbf{z} \right\rangle + \langle M(\mathbf{u}), \mathbf{z} \rangle - \langle B^* p, \mathbf{z} \rangle = \langle \mathbf{f}, \mathbf{z} \rangle, \quad \mathbf{z} \in \mathbf{V}, \quad (45)$$

$$\langle B\mathbf{u}, q \rangle = 0, \quad q \in H. \quad (46)$$

where $\mathbf{V} \subset H^1(\Omega(\alpha))^2$, $H := L^2(\Omega(\alpha))$, and $\langle \cdot, \cdot \rangle$ denotes the dual pairing between \mathbf{V}^* and \mathbf{V} and H^* and H , respectively. Moreover, $F_\varepsilon : \mathbf{V} \times \mathbf{V} \rightarrow \mathbb{R}$ is the functional

$$F_\varepsilon(\mathbf{v}, \mathbf{w}) = 2 \int_{\Omega(\alpha)} b(|\mathbf{E}|, \mu(\mathbf{v}, \mathbf{E})) (\varepsilon + I(\mathbf{w}))^{1/2} dx,$$

$M : \mathbf{V} \rightarrow \mathbf{V}^*$ stands for the nonlinear operator given by

$$\begin{aligned} \langle M(\mathbf{v}), \mathbf{w} \rangle &= 2 \int_{\Omega(\alpha)} \psi(I(\mathbf{v}), |\mathbf{E}|, \mu(\mathbf{v}, \mathbf{E})) \mathbf{D}(\mathbf{v}) : \mathbf{D}(\mathbf{w}) dx. \end{aligned}$$

and $B : \mathbf{V} \rightarrow H^*$ refers to the div operator.

Theorem 2 ([34]) Assume that the functions $b : \mathbb{R}_+ \times [0, 1] \rightarrow \mathbb{R}$ and $\psi : \mathbb{R}_+ \times \mathbb{R}_+ \times [0, 1] \rightarrow \mathbb{R}$ in Eq. 42 are continuous and there exist constants a_i , $1 \leq i \leq 3$, such that

$$\text{(C1)} \quad 0 \leq b(x_1, x_2) \leq a_1,$$

$$\text{(C2)} \quad a_3 \geq \psi(x_1, x_2, x_3) \geq a_2.$$

Moreover, suppose that the function $z \mapsto \psi(z^2, x_2, x_3)z$ is monotonically increasing, i.e.,

$$\text{(C3)} \quad z_1 > z_2 \implies \psi(z_1^2, x_2, x_3)z_1 > \psi(z_2^2, x_2, x_3)z_2.$$

Then, the variational system 45 and 46 admits a solution $(\mathbf{u}, p) \in \mathbf{V} \times H$.

Remark 5 The assumptions (C1), (C2), and (C3) in Theorem 2 are moderate and physically reasonable. In particular, the monotonicity condition (C3) requires increasing shear stress for increasing shear rate.

Assuming a known angle $\mu(\mathbf{u}, \mathbf{E})$ between the velocity vector and the exterior electric field, the flow model 39 and 41 has been discretized in space by $Q_2 - P_1$ Taylor-Hood elements with respect to a simplicial triangulation of a reference computational domain $\Omega(\hat{\alpha})$, where $\hat{\alpha} \in \mathbb{R}^m$ is chosen within the set of feasible design parameters such that $\Omega(\alpha) = \Phi(\Omega(\hat{\alpha}))$. The resulting NLP problem has been solved by the primal-dual Newton interior point method featuring an augmented Lagrangian approach [24] for the solution of the discretized state equations within the optimization loop (for details see [41]).

In case of the compression stage (fluid flow from the lower into the upper fluid chamber) and an applied electric field strength of $|\mathbf{E}| = 1,000$ V/mm, Fig. 11 displays the optimized inlet boundary as a whole (left) and a detail of it (right), where the red curve marks the final optimized configuration. On the other hand, Fig. 12 (left) shows the flow profile in the electrorheological duct connecting the lower and the upper fluid chamber for various electric field strengths. In case of no electric field, one clearly observes the parabolic flow profile typical for Newtonian fluid flow (red curve), whereas for increasing field strength the profile flattens in the middle of the duct (blue curve). According to the Bingham-type flow model, the flat region characterizes solid behavior of the electrorheological fluid (Rheobay TP AI 3565 based on polyurethane). For a particular part of the inlet boundary, Fig. 12 (right) shows the initial configuration (black) and the optimized configurations in case of no electric field (red) and electric field strengths of $|\mathbf{E}| = 500$ V/mm (magenta) as well as $|\mathbf{E}| = 1,000$ V/mm (blue).

We note that the differences between the initial configuration and the optimized configurations are small, but give rise to reductions in the pressure variations between 10 and 20%, depending on the operating conditions.

3.3 Topology optimization of high power electronic devices

We consider the topology optimization of pulse width modulated converter modules that are used in high power electromotors in energy generation, energy transmission, and high technology transportation systems such as high speed trains (cf. Fig. 13). Figure 14 shows the

Fig. 11 Optimized inlet boundary (left) and zoom (right) (the red line marks the final optimized configuration)

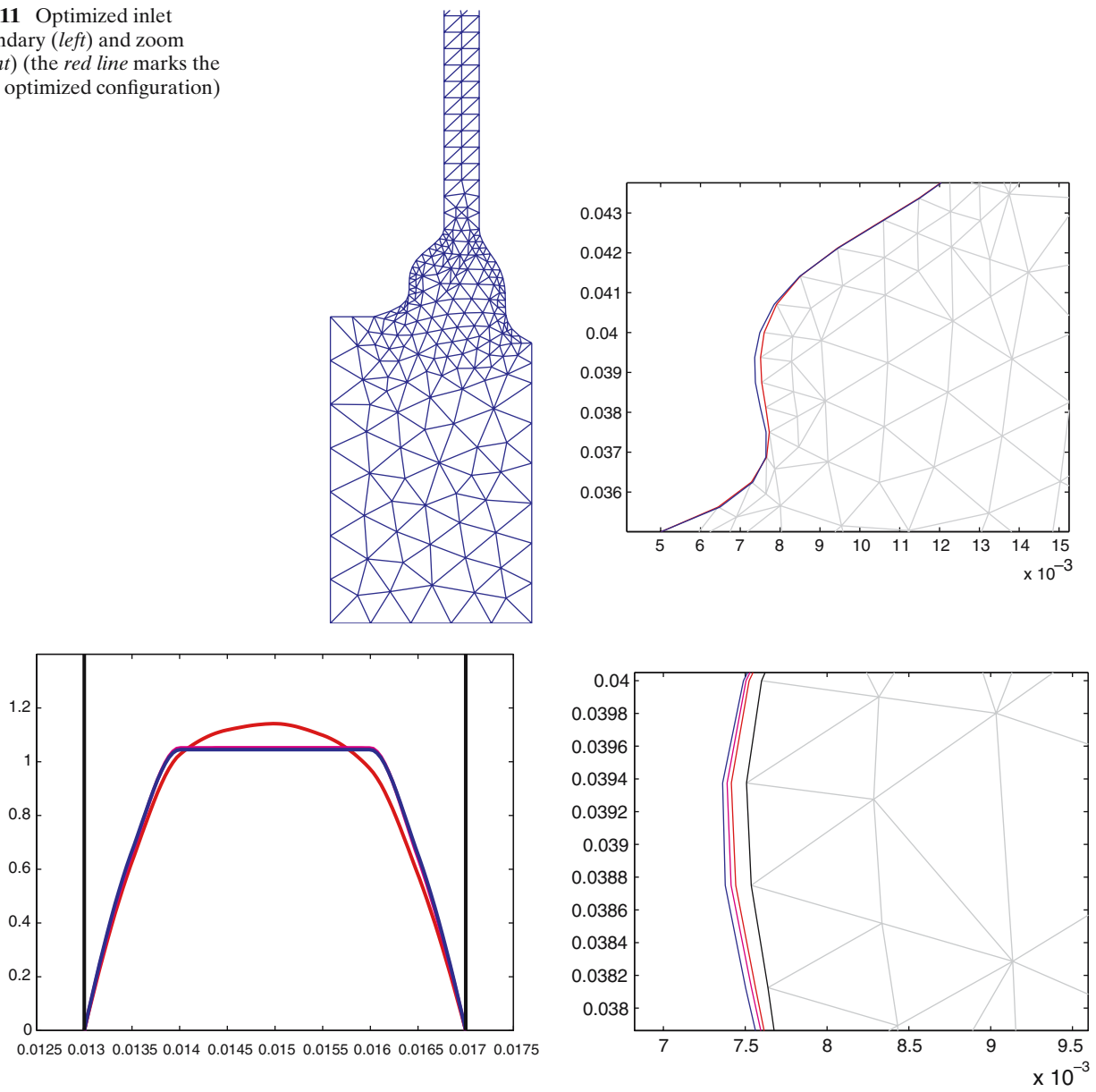


Fig. 12 Flow profile in the ER duct (left) and detail of the optimized inlet boundary for various electric field strengths (right) [red: 0 V/mm, magenta: 500 V/mm, Blue: 1,000 V/mm]



Fig. 13 Applications of converter modules in high power electronics

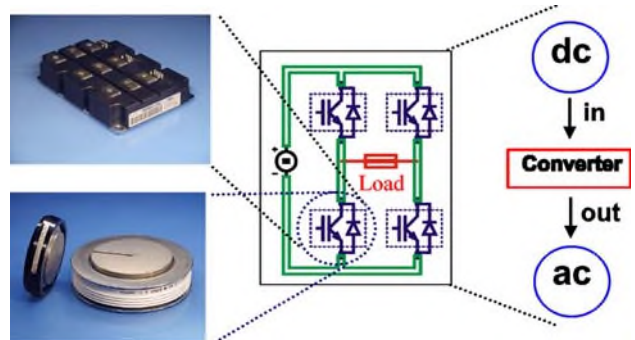


Fig. 14 Schematic representation of a converter module

schematic representation of a converter module consisting of specific semiconductor devices such as insulated gate bipolar transistors (IGBTs) and gate turn off thyristors (GTOs). The IGBTs and GTOs serve as valves for the electric currents in the range of several kilo-ampères featuring switching times of less than 100 ns (cf. [10,11]). They are interconnected and linked with the power source and the electro motor by copper made bus bars.

Figure 15 displays the typical configuration of the bus bars. Each bus bar has N ports where the IGBTs and GTOs are attached to the device. Although high currents and fast switching times can be realized, the problem in the design of the converter modules is that steep current ramps cause the generation of eddy currents in the bus bars leading to parasitic inductivities which result in significant losses in the power transmission. Experimental investigations by the design engineers revealed that placing holes in the bus bars strongly influences the eddy currents and thus helps to reduce the power losses. Therefore, the ultimate problem can be stated as follows: how many holes of which size should be placed where in the bus bars to minimize the parasitic inductivities. In mathematical terms, this design objective can be formulated as a topology optimization problem.

In the sequel, we restrict ourselves to the optimization of a single bus bar occupying a bounded domain $\Omega \subset \mathbb{R}^3$ with N ports $\Gamma_\nu \subset \Gamma$, $1 \leq \nu \leq N$. The operational behavior of a bus bar can be described by the eddy currents equations which we consider in its potential formulation by means of a scalar electric potential φ and a magnetic vector potential \mathbf{A} which satisfy a coupled system of PDEs consisting of an elliptic boundary value for the scalar electric potential in Ω

$$\operatorname{div}(\sigma \operatorname{grad} \varphi) = 0 \quad \text{in } \Omega, \quad (47)$$

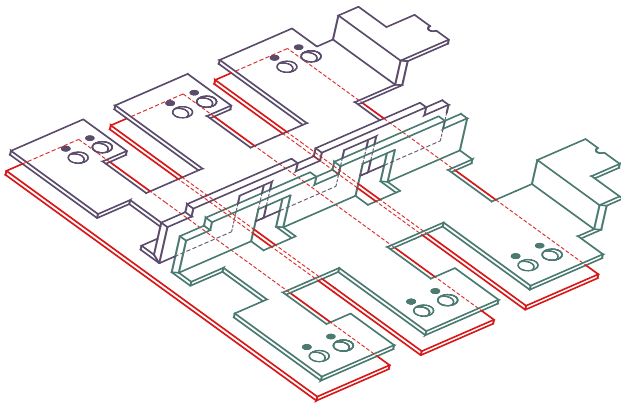


Fig. 15 Typical configuration of bus bars

$$\sigma \mathbf{n} \cdot \operatorname{grad} \varphi = \begin{cases} -I_\nu(t) & \text{on } \Gamma_\nu \\ 0 & \text{else} \end{cases} \quad (48)$$

and a parabolic equation for the double curl operator

$$\sigma \frac{\partial \mathbf{A}}{\partial t} + \operatorname{curl} \mu^{-1} \operatorname{curl} \mathbf{A} = \begin{cases} -\sigma \operatorname{grad} \varphi & \text{in } \Omega \\ 0 & \text{in } \mathbb{R}^3 \setminus \Omega, \end{cases} \quad (49)$$

which has to be considered in the interior and exterior domain together with appropriate boundary, transmission, and initial conditions. Here, σ refers to the electric conductivity, μ denotes the magnetic permeability, and I_ν , $1 \leq \nu \leq N$, are the current densities at the contacts satisfying the compatibility condition

$$\sum_{\nu=1}^N I_\nu(t) = 0.$$

The total inductivity can be described by the functional

$$J(\varphi, \mathbf{A}, \sigma) := \sigma^{-1} \int_0^T \int_{\Omega} f(\varphi, \mathbf{A}) \, dx \, dt, \quad (50)$$

where the integrand f depends on the generated eddy currents in terms of the scalar electric potential and the magnetic vector potential (cf., e.g., [11]).

Choosing the conductivity σ as the design variable, the topology optimization problem reads as follows:

$$\inf_{\varphi, \mathbf{A}, \sigma} J(\varphi, \mathbf{A}, \sigma) \quad (51)$$

subject to the equality constraints

$$\varphi, \mathbf{A} \text{ satisfy Eqs. 47–49} \quad (52)$$

$$\int_{\Omega} \sigma \, dx = C \quad (53)$$

and the inequality constraints

$$\sigma_{\min} \leq \sigma \leq \sigma_{\max}. \quad (54)$$

Remark 6 The equality constraint Eq. 53 prescribes the total amount of material. Without this constraint, the optimization would result in technologically not feasible extremely thin interconnects between the contacts.

Remark 7 The obvious choice of the design variable [either $\sigma = 0$ (no material) or $\sigma = \sigma_{\max}$ (conductivity of copper)] leads to an ill-posed 0-1 optimization problem. Therefore, Eq. 54 represents some sort of relaxation by allowing the design variable to vary between a small positive value $\sigma_{\min} \ll 1$ and the maximum value σ_{\max} . However, to avoid “grey scales” in the design, the extreme values σ_{\min} and σ_{\max} are enforced by the SIMP

method known from topology optimization of mechanical structures (cf., e.g., [67]). The SIMP approach relies on the scaling

$$\eta(\sigma) = \left(\frac{\sigma - \sigma_{\min} + \varepsilon}{\sigma_{\max} - \sigma_{\min}} \right)^m, \quad 0 < \varepsilon \ll 1, \quad (55)$$

with an appropriate penalty parameter $m \geq 1$.

In topology optimization, the finite element discretization of the state equations has to be done with care, since it is well known that lower order conforming elements based on a simplicial triangulation T_h of the computational domain Ω often give rise to checker-board patterns in the design. A convenient remedy is to use either higher order or nonconforming elements. Therefore, as far as the state equations (47–49) are concerned, the potential equations (47) and (48) for the scalar electric potential φ is discretized by the lowest order nonconforming Crouzeix–Raviart elements. For the discretization in time of the parabolic equation (49) for the magnetic vector potential \mathbf{A} we use the backward Euler scheme, whereas the discretization in space is done by means of the lowest order curl-conforming edge elements of Nédélec’s first family (cf. [46]) both in the interior domain and in the exterior domain with an artificial boundary off the device. In the interior domain, the design variable σ is discretized by elementwise constants.

The discretized topology optimization problem represents an equality and inequality constrained NLP and has been solved by the primal-dual Newton interior-point method described in Sect. 2. Within the right transforming iterative scheme for the condensed primal-dual system, the iterative solution of the discretized state equations has been realized by mortar edge element methods involving a domain decomposition approach on nonmatching meshes featuring multigrid preconditioners with hybrid smoothing with respect to adaptively generated hierarchies of simplicial triangulations of the subdomains (cf., e.g., [30,37,38]).

Figure 16 shows the computed material distribution in a 2D test example with two and six ports, respectively. The penalty parameter m in the SIMP method (55) has been chosen according to $m = 2$ in both cases.

Table 3 contains the convergence history of the primal-dual Newton interior-point method for the topology optimization of a single bus bar with the parasitic inductivity as the objective functional. In the table, N_C is the number of contacts (ports), “iter” stands for the number of iterations until convergence, β is the last value of the barrier parameter, $M^{(\beta)}$, \mathcal{F} are the final values of the primary and secondary merit functions, and $\|w\|_2$ is the ℓ_2 -norm of the perturbed complementarity at the last iteration.

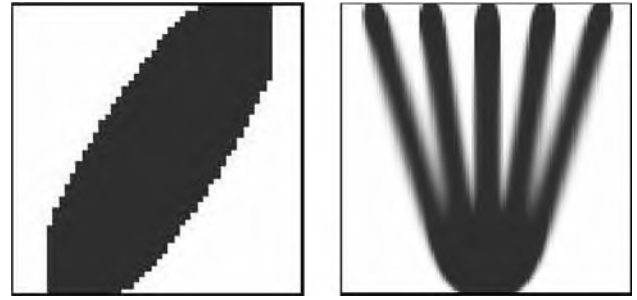


Fig. 16 Optimal material distribution for a 2D test example [two ports (*left*) and six ports (*right*)]

Table 3 Convergence history of the primal-dual Newton interior-point method (topology optimization of bus bars in converter modules)

N_C	iter	β	$M^{(\beta)}$	\mathcal{F}	$\ w\ _2$
2	19	1.97E–17	4.47	3.49E–5	2.27E–09
4	21	7.34E–18	27.29	8.12E–5	4.75E–11
5	22	7.48E–18	79.14	8.45E–4	7.16E–10
6	20	9.85E–17	81.99	1.27E–3	5.62E–09

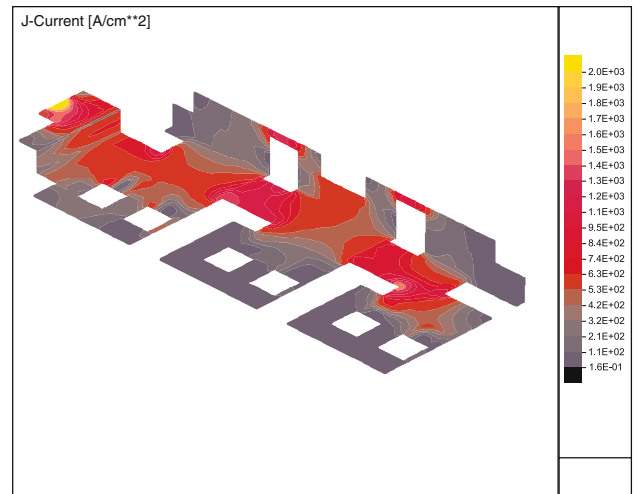


Fig. 17 Distribution of currents in an optimized bus bar

For further results, including the impact of the penalty parameter and the granularity of the triangulations on the final design as well as the history of the iterative solution process, we refer to [35] and [39].

In the 3D case, Fig. 17 shows the distribution of the surface current densities in an optimized single bus bar by a scale ranging from 0.0 kA/cm² (blue) to 2.0 kA/cm² (yellow). The impact of the holes on the generated eddy currents is illustrated in Fig. 18 displaying the computed magnetic vector potential \mathbf{A} (left) and the magnetic induction $\mathbf{B} = \text{curl } \mathbf{A}$ (right) in a vicinity of two ports that are located above the two holes in the lower part of the pictures.

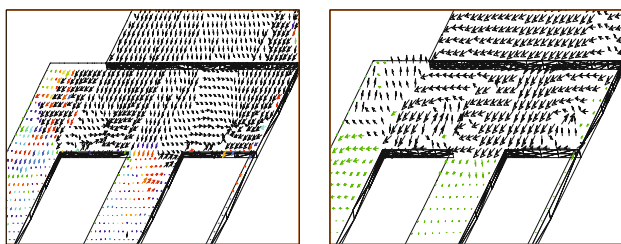


Fig. 18 Magnetic vector potential (*left*) and magnetic induction (*right*)

The application of the primal-dual Newton interior-point method gave rise to a local minimum of the objective functional realizing a reduction of the loss in the power transmission. Depending on the operating conditions, reductions in the range between 20 and 30% could be achieved. Moreover, compared to the traditional design methodology (alternating approach characterized by the solution of the state equations for a given design followed by an update of the design variables based on a sensitivity analysis), the “all-at-once” method turned out to be computationally much more efficient with a reduction of computational times by an order of magnitude.

4 Conclusion

The “all-at-once” approach by primal-dual Newton interior-point methods represents a highly efficient and robust numerical technique for the solution of constrained nonlinear optimization problems with PDE constraints. The simultaneous treatment of the discretized state equations and the design objective within an integrated optimization loop offers decisive computational advantages compared to more traditional strategies, in particular, when the specific structure of the primal-dual Hessian is adequately taken into account. Numerical results for various technologically relevant shape and topology optimization problems in structural mechanics, fluid mechanics, and electromagnetics underline the wide range of applicability.

References

- Allaire, G.: Shape Optimization by the Homogenization Method. Springer, Berlin Heidelberg New York (2002)
- Bayer, A.G.: Provisional Product Information. Rheobay TP AI 3565 and Rheobay TP AI 3566. Bayer AG, Silicones Business Unit, No. AI 12601e, Leverkusen (1997)
- Bendsøe, M.P.: Optimization of Structural Topology, Shape, and Material. Springer, Berlin Heidelberg New York (1995)
- Bendsøe, M.P., Sigmund, O.: Topology Optimization: Theory, Methods and Applications. Springer, Berlin Heidelberg New York (2003)
- Bergounioux, M., Haddou, M., Hintermüller, M., Kunisch, K.: A comparison of a Moreau-Yosida based active set strategy and interior point methods for constrained optimal control problems. *SIAM J. Optim.* **11**, 495–521 (2000)
- Bertsekas, D.P.: Constrained Optimization and Lagrange Multiplier Methods. Academic, New York, (1982)
- Biros, G., Ghattas, O.: Parallel Lagrange–Newton–Krylov–Schur methods for PDE constrained optimization. part I: The Krylov–Schur solver. *SIAM J. Sci. Comput.* **27**, 687–713 (2005a)
- Biros, G., Ghattas, O.: Parallel Lagrange–Newton–Krylov–Schur methods for PDE constrained optimization. Part I: The Lagrange–Newton solver and its application to optimal control of steady viscous flows. *SIAM J. Sci. Comput.* **27**, 714–739 (2005b)
- Boggs, P.T., Tolle, J.W.: Sequential quadratic programming. *Acta Numer.* **4**, 1–50 (1995)
- Böhm, P., Wachutka, G., Hoppe, R.H.W.: Modeling and simulation of the transient electromagnetic behavior of high power bus bars. In: High Performance Scientific and Engineering Computing, Methods, Developments, and Applications, Proc. Int. FORTWIHR Conf. 2001, Erlangen, March 12–14, 2001 (Durst, F., Zenger, Chr. (eds.), Lecture Notes in Computational Science and Engineering, pp. 385–392 Springer **21**, Berlin Heidelberg New York (2002)
- Böhm, P., Hoppe, R.H.W., Mazurkevitch, G., Petrova, S., Wachutka, G., Wolfgang, E.: Optimal structural design of high power electronic devices by topology optimization. In: Krebs, H., Jäger, W. (eds.), Mathematics Key Technology for the Future. Cooperations between Mathematics and Industry, pp. 365–376, Springer, Berlin Heidelberg New York (2003)
- Chamberlain, R.M., Lemaréchal, C., Pedersen, H.C., Powell, M.J.D.: The watchdog technique for forcing convergence in algorithms for constrained optimization. *Math. Programming Study* **16**, 1–17 (1982)
- Cherkaev, A.: Variational Methods for Structural Optimization. Springer, Berlin New York (2000)
- Delfour, M.C., Zolesio, J.P.: Shapes and Geometries: Analysis, Differential Calculus and Optimization. SIAM, Philadelphia (2001)
- Dennis, J., Heinkenschloss, M., Vicente, L.N.: Trust-region interior-point SQP algorithms for a class of nonlinear programming problems. *SIAM J. Control Optim.* **36**, 1750–1794 (1998)
- Deuffhard, P.: Newton Methods for Nonlinear Problems. Affine Invariance and Adaptive Algorithms. Springer, Berlin Heidelberg New York (2004)
- Engelmann, B., Hiptmair, R., Hoppe, R.H.W., Mazurkevitch, G.: Numerical simulation of electrorheological fluids based on an extended Bingham model. *Comput. Vis. Sci.* **2**, 211–219 (2000)
- Fiacco, A.V., McCormick, G.P.: Nonlinear Programming: sequential Unconstrained Minimization Techniques. Reprint, SIAM, Philadelphia (1990)
- Filisko, F.: Overview of ER technology. In: Havelka, K.:(ed.), Progress in ER Technology. Plenum Press, New York (1995)
- Forsgren, A., Gill, Ph.E., Wright, M.H.: Interior methods for nonlinear optimization. *SIAM Rev.* **44**, 522–597 (2002)
- Gay, D.M., Overton, M.I., Wright, M.H.: Primal-dual interior method for nonconvex nonlinear programming. In: Yuan, Y., (ed.) Advances in Nonlinear Programming, pp. 31–56, Kluwer, Dordrecht (1998)
- Gill, Ph.E., Murray, W., Saunders, M.A., Tomlin, J.A., Wright, M.H.: On projected Newton barrier methods for linear programming and an equivalence to Karmarkar’s projective method. *Math. Program.* **36**, 183–209 (1986)

23. Gill, Ph.E., Murray, W., Wright, M.H.: Practical Optimization. Reprint, Academic, New York (1999)
24. Glowinski, R., LeTallec, P.: Augmented Lagrangian and Operator-Splitting Methods in Nonlinear Mechanics. SIAM Studies in Applied Mathematics, vol. 9, SIAM, Philadelphia (1989)
25. Greil, P., Lifka, Th., Kaindl, A.: Biomorph cellular silicon carbide ceramics from wood: I. Processing and microstructure. *J. Eur. Ceram. Soc.* **18**, 1961–1973 (1998a)
26. Greil, P., Lifka, Th., Kaindl, A.: Biomorph cellular silicon carbide ceramics from wood: II. Mechanical properties. *J. Eur. Ceram. Soc.* **18**, 1975–1983 (1998b)
27. Haslinger, J., Mäkinen, R.A.E.: Introduction to Shape Optimization: Theory, Approximation, and Computation. SIAM, Philadelphia (2004)
28. Haslinger, J., Neittaanmäki, P.: Finite Element Approximation for Optimal Shape Design: Theory and Applications. Wiley, Chichester (1988)
29. Hintermüller, M.: A primal-dual active set algorithm for bilaterally control constrained optimal control problems. *Quar. Appl. Math.*, **LXI**, 131–161 (2003)
30. Hoppe, R.H.W.: Adaptive domain decomposition techniques in electromagnetic field computation and electrothermomechanical coupling problems. In: Brezzi F. et al., (eds.) Proc. 4th European Conference on Numerical Mathematics and Advanced Applications, Ischia, Italy, July 23–27, 2001, pp. 201–218, Springer, (2003)
31. Hoppe, R.H.W., Petrova, S.I.: Homogenized elasticity solvers for biomorph microcellular ceramics. In: Brezzi, F. et al. (eds.) Proc. 4th Europ. Conf. Numer. Math. and Adv. Appl., ENUMATH 2001, July 23–28, 2001, Ischia, Italy, pp. 371–380, Springer Berlin Heidelberg New York (2003a)
32. Hoppe, R.H.W., Petrova, S.I.: Homogenization design method for biomorph composite materials. *J. Comput. Methods Sci. Eng.* **3**, 383–391 (2003b)
33. Hoppe, R.H.W., Petrova, S.I.: Applications of primal-dual interior methods in structural optimization. *Comput. Methods Appl. Math.* **3**, 159–176 (2003c)
34. Hoppe, R.H.W., Litvinov, W.G.: Problems on electrorheological fluid flow. *Commun. Pure Appl. Anal.* **3**, 809–848 (2004a)
35. Hoppe, R.H.W., Petrova, S.I.: Primal-dual Newton interior point methods in shape and topology optimization. *Numer. Linear Algebra Appl.* **11** 413–429 (2004b)
36. Hoppe, R.H.W., Petrova, S.I.: Optimal shape design in biomimetics based on homogenization and adaptivity. *Math. Comput. Simulat.* **65** 257–272 (2004c)
37. Hoppe, R.H.W., Petrova, S.I., Schulz, V.: Topology optimization of high power electronic devices. In: Hoffmann, K.-H., Leugering, G. et al. (eds.) Proc. Conf. Oberwolfach Conference "Optimal Control and Optimization", Oberwolfach, June 5–9, 2000 pp. 119–131, Birkhäuser, Basel (2002a)
38. Hoppe, R.H.W., Petrova, S.I., Schulz, V.: 3D structural optimization in electromagnetics. In: Debit N. et al. (eds.) Proc. 13th Int. Conf. "Domain Decomposition Methods and Applications", Lyon, October 9–12, 2000, pp. 479–486, CIMNE, Barcelona (2002b)
39. Hoppe, R.H.W., Petrova, S.I., Schulz, V.: A primal-dual Newton-type interior-point method for topology optimization. *J. Optim. Theory Appl.* **114**, 545–571 (2002c)
40. Hoppe, R.H.W., Kladny, R., Petrova, S.I., Sieber, H.: Modeling, simulation, and optimization of microstructured biomorph materials. In: Hoffmann, K.H., (ed.), Functional Micro- and Nanosystems. Proceedings of the 4th caesarium, Bonn, June 16–18, 2003 Springer, Berlin Heidelberg New York (2004a)
41. Hoppe, R.H.W., Litvinov, W.G., Rahman, T.: Mathematical modeling and numerical simulation of electrorheological devices and systems. In: Heikkola, E., Kuznetsov, Y., Neittaanmäki, P., Pironneau, O. (eds.) Numerical Methods for Scientific Computing, Variational Problems, and Applications, pp. 80–93. International Center for Numerical Methods in Engineering (CIMNE), Barcelona (2004)
42. Hoppe, R.H.W., Petrova, S.I., Vassilevski, Y.: Adaptive grid refinement for computation of the homogenized elasticity tensor. In: Lirkov, I., et al. (ed.) Proceedings of 4th International Conference on Large Scale Scientific Computing LSSC'03, Sozopol, June 4–8, 2003. Lecture Notes in Computer Science, Vol. 2907, pp. 371–378. Springer, Berlin Heidelberg New York (2004)
43. Karmarkar, N.K.: A new polynomial time algorithm for linear programming. *Combinatorica* **4**, 373–395 (1984)
44. Maar, B., Schulz, V.: Interior point multigrid methods for topology optimization. *Struct. Optim.* **19**, 214–224 (2000)
45. Mohammadi, B., Pironneau, O.: Applied Shape Optimization for Fluids. Oxford University Press, Oxford (2001)
46. Nédélec, J.-C.: Mixed finite element in \mathbb{R}^3 . *Numer. Math.* **35**, 315–341 (1980)
47. Nocedal, J., Wright, S.J.: Numerical Optimization. Springer, Berlin Heidelberg New York (1999)
48. Pironneau, O.: Optimal Shape Design for Elliptic Systems. Springer, Berlin Heidelberg New York (1984)
49. Rajagopal, K., Wineman, A.: Flow of electrorheological materials. *Acta Mechanica* **91**, 57–75 (1992)
50. Rozvany, G.: Structural Design via Optimality Criteria. Kluwer, Dordrecht (1989)
51. Ruge, J.W., Stüben, K.: Algebraic multigrid (AMG). In: McCormick, S.F. (ed.), Multigrid Methods, Frontiers in Applied Mathematics, vol. 5, SIAM, Philadelphia (1986)
52. Růžička, M.: Electrorheological Fluids: Modeling and Mathematical Theory. Lecture Notes in Mathematics, vol. 1748, Springer, Berlin Heidelberg New York (2000)
53. Shenoy, A.R., Heinkenschloss, M., Cliff, E.M.: Airfoil design by an all-at-once approach. *Int. J. Comput. Fluid Mech* **11**, 3–25 (1998)
54. Sieber, H., Rambo, C.R., Cao, J., Vogli, E., Greil, P.: Manufacturing of porous oxide ceramics by replication of wood morphologies *Key. Eng. Mater.* **206–213**, 2009–2012 (2002)
55. Sokolowski, J., Zolesio, J.P.: Introduction to Shape Optimization. Springer, Berlin-Heidelberg-New York (1992)
56. Ulbrich, M.: Semismooth Newton methods for operator equations in functions spaces. *SIAM J. Optim.* **13**, 805–842 (2003)
57. Ulbrich, M., Ulbrich, S.: Superlinear convergence of affine-scaling interior-point Newton methods for infinite-dimensional nonlinear problems with pointwise bounds. *SIAM J. Control Optim.* **38**, 1938–1984 (2000)
58. Ulbrich, M., Ulbrich, S., Heinkenschloss, M.: Global convergence of trust-region interior-point algorithms for infinite-dimensional nonconvex minimization subject to pointwise bounds. *SIAM J. Control Optimization* **37**, 731–764 (1999)
59. Varela-Feria, F.M., Martınez-Fernandez, J., de Arellano-Lopez, A.R., Singh, M.: Low density biomorph silicon carbide: microstructure and mechanical properties. *J. Europ. Ceram. Soc.* **22**, 2719 (2002)
60. Vogli, E., Sieber, H., Greil, P.: Biomorph SiC-ceramic prepared by Si-gas phase infiltration of wood. *J. Eur. Ceram. Soc.* **22**, 2663–2668 (2002)
61. Weiser, M.: Interior point methods in function space. ZIB Report 03-35, Konrad-Zuse-Zentrum für Informationstechnik Berlin (2003)
62. Weiser, M., Deuffhard, P.: The central path towards the numerical solution of optimal control problems. ZIB Report 01-12, Konrad-Zuse-Zentrum für Informationstechnik Berlin (2001)

63. Wittum, G.: On the convergence of multigrid iterations with transforming smoothers. Theory with applications to the Navier Stokes equations. *Numer. Math.* **57**, 15–38 (1989)
64. Wright, M.H.: Interior methods for constrained optimization. *Acta Numer.* **1**, 341–407 (1992)
65. Wright, S.J.: *Primal-Dual Interior-Point Methods*. SIAM, Philadelphia (1997)
66. Ye, Y.: *Interior-Point Algorithm: Theory and Analysis*. Wiley, New York 1997
67. Zhou, M., Rozvany, G.: The COC algorithm, part II: Topological, geometry and generalized shape optimization. *Comp. Meth. Appl. Mech. Engrg.* **89**, 309–336 (1991)
68. Zollfrank, C., Kladny, R., Sieber, H., Greil, P.: Biomorphous SiOC/C-ceramic composites from chemically modified wood templates. *J. Eur. Ceram. Soc.* **24**, 479–487 (2004)